

Article

An Experimental Investigation on the NO and CO Emission Characteristics of a Swirl Convergent-Divergent Nozzle at Elevated Pressure

Zhongya Xi *, Zhongguang Fu, Xiaotian Hu, Syed Waqas Sabir  and Yibo Jiang

National Thermal Power Engineering & Technology Research Center, North China Electric Power University, Beijing 102206, China; fzg@ncepu.edu.cn (Z.F.); huxt@ncepu.edu.cn (X.H.); engr.waqasshah@hotmail.com (S.W.S.); jiangyb@ncepu.edu.cn (Y.J.)

* Correspondence: xizhongya1022@163.com; Tel.: +86-10-6177-2361

Received: 8 May 2018; Accepted: 31 May 2018; Published: 31 May 2018



Abstract: The behavior of the pollutants NO and CO at elevated combustor pressure are of special importance due to the continuing trend toward developing engines operating at higher pressure ratios to yield higher thermal efficiency. An experiment was performed to examine the NO and CO emissions for a swirl convergent-divergent nozzle at elevated pressure. The NO and CO correlations were obtained. Meanwhile, the flame length, exhaust gas oxygen concentration, exit temperature and global flame residence time were also determined to analyze the NO and CO emission characteristics. The results showed that, with the increase in combustor pressure P , flame length decreased proportionally to $P^{-0.49}$; exit O_2 volume fraction increased and exit temperature was reduced. The global flame residence time decreased proportionally to $P^{-0.43}$. As pressure increased, the NO and Emission Index of NO (EINO) levels decreased proportionally to $P^{-0.53}$ and $P^{-0.6}$ respectively, which is mainly attributed to the influence of global flame residence time; the NO and EINO increased almost proportionally with the increase in global flame residence time. The EINO scaling EINO ($\rho u_e/d$) was proportional to $Fr^{0.42}$, which indicated that compared with pure fuel, the fuel diluted with primary air can cause a decrease in the exponent of the Fr power function. At higher pressure, the CO and Emission Index of CO (EICO) decreased proportionally to $P^{-0.35}$ and $P^{-0.4}$, respectively, due to the increased unburned methane and high pressure which accelerated chemical reaction kinetics to promote the conversion of CO to CO_2 .

Keywords: NO emission; CO emission; swirl convergent-divergent nozzle; combustion at elevated pressure; turbulent non-premixed flame

1. Introduction

Pollutant emissions from the combustion of fossil fuels have become great public concern due to their harmful effects on human health and the environment [1]. The regulations for pollutant emissions are becoming increasingly strict, which has recently led combustion devices manufacturers to develop combustors that meet various regulatory requirements.

Gas turbines are critical facilities in the gas and oil industry. The principal pollutants generated by gas turbines are NO and CO, and both emissions have drawn considerable academic interest, particularly in their formation mechanisms and influencing factors. NO could be formed by four different pathways: thermal NO, prompt NO, nitrous oxide NO, and fuel NO [2]. Concerning CO, it arises mainly from incomplete combustion of the fuel, due to inadequate reaction rates in the flame zone caused by very low equivalence ratio and/or insufficient residence time. The factors influencing both NO and CO emissions, e.g., equivalence ratio, flow velocity, fuel property, variable geometry, ambient air temperature have been investigated widely, as mentioned in [3].

Among various impacts, the influence of combustion pressure P on NO and CO formation is of particular significance, because of the continuing trend toward engines with higher pressure ratios (relative to the atmosphere) for achieving higher thermal efficiency and lower fuel consumption [4]. Pressure ratios of heavy-duty gas turbines (F/G/H level) have been increased to about 15~40-fold, such as GE 7HA/9HA (22), Siemens SGT6-6000G/SGT5-8000H (19), Mitsubishi M501G/M701G (20) and M501H (25), ALSTOM GT26 (33).

However, owing to experimental difficulties, combustor measurement data under high pressures is extremely limited [3,5–7]. The vast majority of combustion tests were carried out at low pressure levels, and the results obtained then extrapolated to higher pressure levels. The extrapolation could be performed confidently assuming that the relationship between pollutant emissions and pressure were precisely known. Regrettably, the testing data obtained on various combustor categories are inconsistent in this regard.

In the last few years, a few studies have been performed to explore the effect of combustion pressure on NO and CO emissions in gas turbine combustors. Correa [8] conducted a review to summarize NO_x formation under gas turbine conditions (NO_x consists of NO and NO₂, where the dominant component at high emission levels is NO). The results from his study showed that NO_x and CO emissions scaled proportionally with a power function of the combustion pressure P^n . The exponent n could be swayed by some factors, for example, n approached 0 at low equivalence ratios and was greater than 0 for rich flames. Bhargava et al. [9] carried out experiments and PSR network simulations in the lean conditions range with two different nozzles; the pressure was varied from 100 psi to 400 psi. The results revealed that the NO_x exponent n changed from -0.18 to 1.6 for the tangential nozzle and from -0.77 to 0.61 for the axial nozzle as the equivalence ratio varied from 0.43 to 0.65. Göke et al. [10] studied NO_x and CO emissions for a premixed natural gas flame within a pressure range of 1.5–9.0 bar by performing experiments and simulations. They found that NO_x increased and CO decreased with increasing pressure, the exponent for NO_x emissions increased with equivalence ratio from 0.1 to 0.65 while the exponent for CO emissions was about -0.4 at lower temperatures and -0.5 at higher temperatures. The calculation results in Wang et al. [11] and Pillier et al. [12] also revealed that the NO has an increasing trend but CO has a decreasing trend with pressure.

Nevertheless, when Rutar [13] studied NO_x and CO emissions at an elevated pressure of 3.0–6.5 atm he concluded that NO_x decreased a little with increasing pressure for a fixed residence time, which was also revealed by Steele et al. [14]. Biagioli and Güthe [15] analyzed the NO from 1–30 bar based on a model, and they found that the NO_x pressure exponent is negative under fully premixed conditions. Leonard et al. [16] measured NO_x emissions for well-premixed flames; they pointed out that NO_x emissions were independent of pressure and it is possible to run a combustor from 1 atm to 30 atm without any noticeable change in NO_x emissions.

To investigate the parameters controlling NO_x yields, Røkke et al. [17] proposed a leading-order scaling approach for buoyancy-dominated hydrocarbon non-premixed flames based on simplified expressions for the flame volume, simplified finite-rate reaction mechanism, and a flamelet description which includes hydrocarbon fuel components up to C₃. They proposed a theoretical expression to predict the NO_x emission index EINO_x, i.e., Equation (1):

$$\text{EINO}_x(\rho u_e/d) \propto Fr^{0.6} \quad (1)$$

where ρ stands for the fuel jet density; u_e represents fuel jet exit velocity; d stands for the diameter of nozzle exit; Fr represents the jet exit Froude number, which is defined by Equation (2):

$$Fr = u_e^2/gd \quad (2)$$

where g is the acceleration of gravity.

The NO_x emission index EINO_x is defined as the ratio of the mass rate of NO produced to the mass of fuel supplied, as given by Equation (3) [18]:

$$\text{EINO}_x = \dot{m}_{\text{NO}_x} / \dot{m}_F \quad (3)$$

Equation (1) was used to predict their experimental data as well as data from other researches for hydrocarbon fuels [19–22]. Generally, the predicted results were good for Fr less than 10^5 . Moreover, Szegö et al. [23] explored the impacts of diluent on EINO_x for a laboratory-scale mild combustor. It was found that the exponential constant for Fr^n varied with the addition of N_2 or CO_2 into fuel compared to fuel with no diluents.

To predict combustion emissions based on a set of operating parameters, e.g., fuel composition, combustor pressure, air flow rate, equivalence ratio, inlet air temperature, some empirical and semi-empirical models are widely employed. These models are developed by correlating test data on pollutant emissions in terms of all the relevant parameters. They serve in designing and developing low-emission combustors by reducing the complicated problems affiliated with emissions to forms which are more easier for the combustion engineers. These models can be found in the reviews by Tsalavoutas et al. [24], Chandrasekaran and Guha [25], as listed in Table A1 in Appendix A. For example, a general correlation proposed by Lefebvre [26] is showed by Equation (4):

$$\text{EINO}_x = 0.459 \times 10^{-8} P^{0.25} \cdot F \cdot \tau \cdot \exp(0.01T_{st}) \quad (4)$$

where F is the fraction of air employed in the flame zone; τ is the flame zone residence time, (measured in s); T_{st} is the stoichiometric flame temperature, (measured in K). Equation (4) considers the fact that in the combustion of heterogeneous fuel-air mixtures, the formation of NO_x is determined by the stoichiometric flame temperature T_{st} , rather than the average flame temperature. However, the residence time in the flame zone τ is also important to NO_x formation. Another example proposed by Røkke et al. [27] is displayed by Equation (5):

$$\text{EINO}_x = 1.46 P^{1.42} \dot{m}_{air}^{0.3} f_{far}^{0.72} \quad (5)$$

where \dot{m}_{air} is air mass flow rate, f_{far} is fuel to air ratio. The influence of combustion temperature on NO_x is considered by the inclusion of the fuel to air ratio f_{far} .

Recently, several correlations were obtained for specific industrial combustors: a correlation for a model combustor of an aero gas turbine by Li et al. [28], a correlation for fuel staged combustion employing laboratory-scale gas turbine combustor by Han et al. [7], and another correlation for a 10 MW non-premixed gas turbine combustor utilizing high hydrogen fuels by Kroniger and Wirsum [29].

It can be concluded from the above that the NO and CO behavior at high pressure is variable and even contradictory in different tests. NO increased, decreased or even remained unaffected by pressure for different burners/combustors, correspondingly, the pressure exponent for NO was positive, negative or even zero. The emissions test data at high-pressure were rare, and the effects of pressure on them are comparatively unknown. Meanwhile, the proposed NO correlations are strongly dependent on the specific burners/combustors and combustion technology. An individual NO correlation could not be used to estimate NO emissions accurately for a particular combustion device. Lastly, the EINO scaling with Fr was not yet examined with the addition of primary air in fuel. Therefore, further exploration is needed to reveal the NO and CO characteristics at elevated pressure.

In this paper, a swirl convergent-divergent nozzle designed for high flame stability and low pollutants emissions was examined experimentally regarding NO and CO emissions at elevated combustor pressure for turbulent non-premixed combustion. The flame zone, exit O_2 volumetric fraction, exit temperature were also measured to analyze the emissions characteristics. The CO and NO correlations were obtained by fitting the test data, the EINO scaling with Fr was also presented.

2. Experimental Setup

2.1. Experimental Apparatus

The swirl convergent-divergent nozzle design used in our efforts was mainly based on the combination of swirl combustion technology and divergent conical nozzle technology, as shown in Figure 1a, with an endeavor to enhance the flame stabilization and lowering pollutants emission. The swirl generated by the swirler can strengthen flame stabilizing, control flame size and combustion intensity, decrease NO formation by improving the mixing of fuel and air [30–32]. The divergent conical nozzle technology can obtain highly stabilized flames which can be seen in previous studies [33–36]. Moreover, the convergent passage can further enrich the mixing of fuel and air to lower the pollutant emissions. The nozzle mainly consists of three components: the central fuel tube, the swirler, and the convergent-divergent passage. The swirler is the radial type and has 10 straight vanes, as shown in Figure 1b, the setting angle of vanes α is 50° . The angle between the divergent side face of the nozzle and vertical line is 42° .

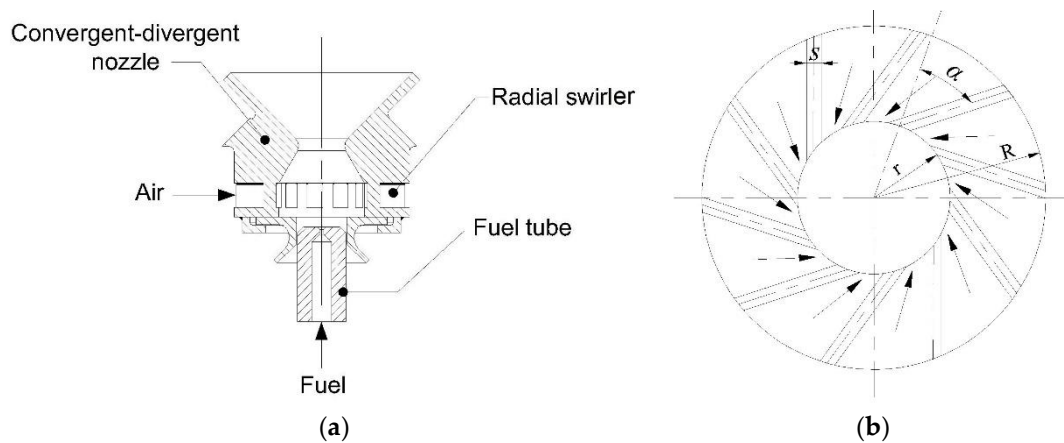


Figure 1. (a) Swirl convergent-divergent nozzle; (b) swirler.

For the present investigation, a 20 kW high-pressure combustion test rig was installed, which can be run at pressures less than 2 Mpa, as shown in Figure 2.

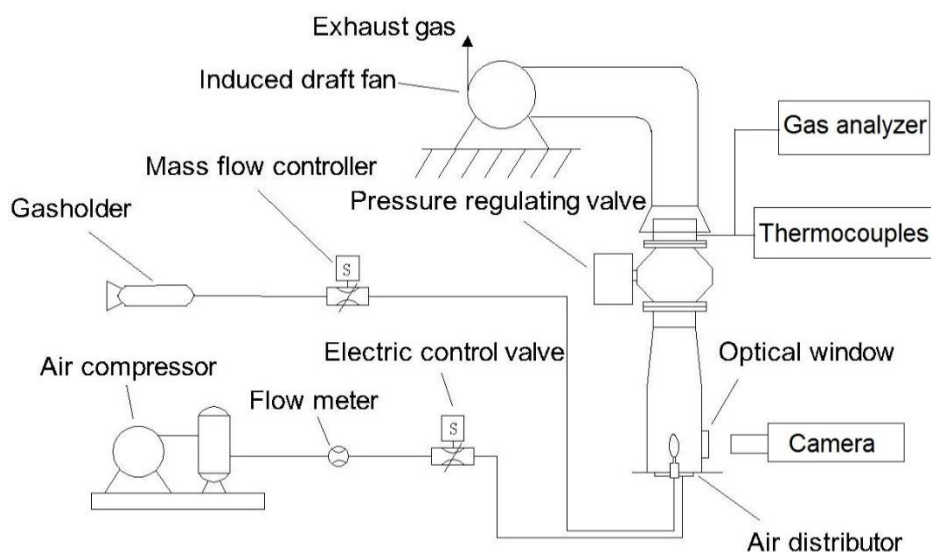


Figure 2. The schematic diagram of high-pressure combustion test rig.

It is composed mainly of three sections: the supply section, the combustion chamber and the exhaust section, which are described as follows:

(1) The supply section, in which an air compressor is used to supply air, the air mass flow rate has a maximum of 2.5 kg/min. The air is regulated electrically through a control valve and measured using an air flow meter. A gas holder is employed to provide the fuel, which is methane. The fuel is regulated and measured by a mass flow controller (MFC), the fuel mass flow rate has a maximum of 36 g/min.

(2) The combustion chamber, which is an axisymmetric cylindrical chamber, its diameter is 0.3 m and height is 1.35 m, as shown in Figure 3. This combustion chamber is mainly composed of four components: swirl convergent-divergent nozzle, wind distributing plate, cooling slot near to the inner wall, and combustor. The swirl convergent-divergent nozzle has been previously displayed in Figure 1b. A part of the air flows tangentially through the swirler to bring the fuel provided with the central fuel tube into the combustor in which burning occurs (initiated by an igniter near the nozzle). This part of air is referred as primary air, which is 5% of total inlet air by mass fraction, it is used to mix with methane before combustion for controlling flame length. The mixing degree of primary air and methane is incomplete since the distance for mixing is relatively short. The rest of the air flows through air wind distribution plate to a cooling slot near to the inner wall, and then enters into the combustor. This part of the air is referred as secondary air, and is used to support combustion and cool the wall to avoid heat damage to the metal material. An optically accessible window is installed on the combustor wall that can be used to observe the flame structure.

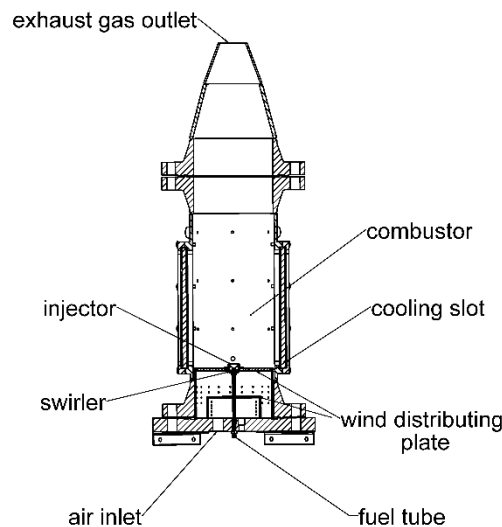


Figure 3. The combustion chamber.

(3) The exhaust section, which is mainly composed of a pressure controlling valve and induced draught system. The pressure controlling valve is used for regulating the combustor operating pressure. The induced draught system is used for expelling the exhaust gas to the atmospheric environment. Besides, there are some mounting bases installed on the exhaust section to allow the measurements of exit gas composition and exit temperature.

2.2. Measurement Methods

Flame appearance was determined by measuring the CO_2^* chemiluminescence image through the optical window, with a high-speed camera (*i* speed 3, Olympus, Essex, UK) coupled to an optical filter (BG 38, HB-OPTICAL, Shengyang, China) which has a bandwidth of 340–600 nm, as displayed in Figure 4.

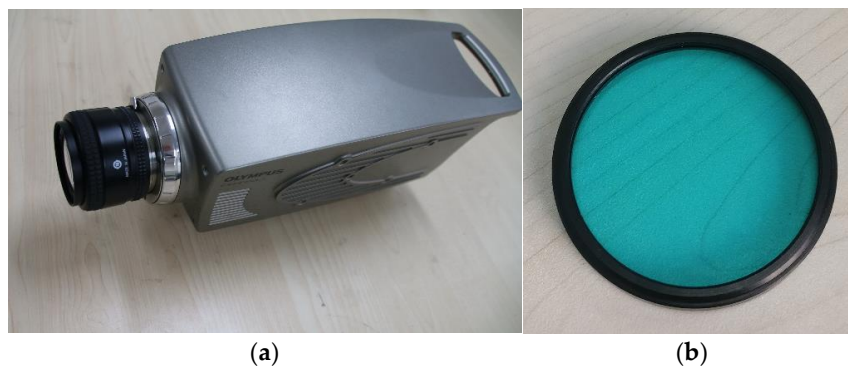


Figure 4. Flame zone recording instruments: (a) high-speed camera; (b) optical filter.

The CO_2^* method is often used for determining flame zones, which can be seen in the previous studies reviewed by Samaniego et al. [37]. Although within the 340–600 nm wavelength range several species such as PAH, CH, C, etc., exist, their influence can be neglected as CO_2^* is the main emitter in hydrocarbon flames. As the review [37] indicated, the amount of CO_2^* emissions is more than 95% of the total chemiluminescence integrated over the whole 340–600 nm range, therefore, the effect of chemiluminescence signals from other species could be ignored in comparison with CO_2^* emissions. As an indicator of the flame zone, the CO_2^* formation consists of three elementary steps, given in Equation (6) [37]:



The CO_2^* is produced by the first step reaction, which is a three-body reaction. In the second and third step reaction, CO_2^* returns to its ground state. The second step reaction is the cause of the CO_2^* light emission and competes with the third step reaction which is a quenching step.

The recording frame rate of the camera was 400 frames per second. At each case, an averaged flame image was acquired by averaging a total of 800 consecutive instantaneous images. The averaged image was then employed to determine the flame shape and size. The combustor pressure was measured with a pressure transmitter mounted on the chamber wall. Exit temperature was measured by the K-type thermocouples placed along the radius (for mean values) at the exhaust gas exit. Exhaust gas was extracted with a probe located downstream of the exhaust nozzle; NO, CO, O_2 were measured with a testo350 gas analyzer (TestoSE & Co. KGaA, Badenia-wirtembergia, Germany), as displayed in Figure 5.



Figure 5. Gas analyzer.

O₂ was employed to correct the NO and CO emissions under standard 15% oxygen concentration. The delay between the sample probe and analyzer required a steady flame be held in each test case for approximately 60 seconds before a steady measurement could be attained. The instrument specifications and measurement uncertainty according to the manufacturer are shown in Table 1.

Table 1. Specifications of the instrument and uncertainty.

Measurement	Instrument	Range	Accuracy	Uncertainty
Temperature	K-type thermocouple	273–1273 K	±1 K	± 1 K
O ₂	Testo 350 gas analyzer	0–25 vol %	±0.8% FSR	0.01 vol %
CO	Testo 350 gas analyzer	0–500 ppm	±2 ppm (0–39.9 ppm) ±5% (40–500 ppm)	0.1 ppm
NO	Testo 350 gas analyzer	0–300 ppm	±2 ppm (0–39.9 ppm), ±5% (40–300 ppm)	± 0.1 ppm

2.3. Experimental Conditions

Test cases are shown in Table 2. Operating pressure P was increased from 3 bar to 6 bar; fuel mass flow rate \dot{m}_F was varied from 12–16 g/min at a fixed pressure, air mass flow rate and primary air mass flow rate \dot{m}_{pri} were kept constant for all cases.

Table 2. Operating conditions of the experiment.

Case	Combustor Pressure, P (bar)	Methane Mass Flow Rate, \dot{m}_F (g/min)	Air Mass Flow Rate, \dot{m}_A (kg/min)	Primary Air, \dot{m}_{pri} (g/min)	\dot{m}_F/\dot{m}_{pri}
1	3	12	2.1	105	0.114
2	3	14	2.1	105	0.133
3	3	16	2.1	105	0.152
4	4	12	2.1	105	0.114
5	4	14	2.1	105	0.133
6	4	16	2.1	105	0.152
7	5	12	2.1	105	0.114
8	5	14	2.1	105	0.133
9	5	16	2.1	105	0.152
10	6	12	2.1	105	0.114
11	6	14	2.1	105	0.133
12	6	16	2.1	105	0.152

3. Results and Discussion

3.1. Flame Shape and Length

Figure 6 displays flame appearances for combustor pressure P under varying \dot{m}_F/\dot{m}_{pri} ratios; it should be noted that the flame base is the nozzle divergent end. One can see that the flame shape became shorter and the flame volume decreased with the increment of P at a fixed \dot{m}_F/\dot{m}_{pri} ratio, the same phenomenon was also detected in [38]. It could be associated with the declined axial diffusion of fuel under higher pressure. It can also be seen in Figure 6 that the flame zone became longer and wider as the \dot{m}_F/\dot{m}_{pri} ratio increased at a given P , which could be attributed to the augmented ambient air that needed to be entrained to reach stoichiometric proportions. The flame length L_f is defined as the distance from nozzle throat to flame tip, since the throat is treated as the nozzle injection exit, so, the L_f can be obtained by summing the measuring length and the length between the nozzle divergent end and the throat.

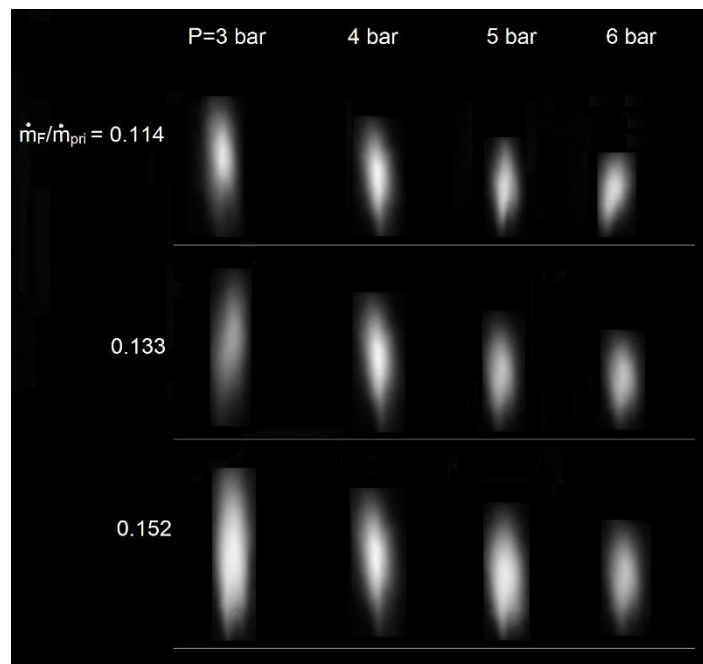


Figure 6. Flame shape for combustor pressure under different $\dot{m}_F / \dot{m}_{pri}$ ratios.

Figure 7 shows L_f shortened with the increasing P at a fixed $\dot{m}_F / \dot{m}_{pri}$ ratio but enlarged with the increment of $\dot{m}_F / \dot{m}_{pri}$ ratio. The L_f was influenced significantly by P and $\dot{m}_F / \dot{m}_{pri}$ with an opposite effect. By fitting the L_f data against P and $\dot{m}_F / \dot{m}_{pri}$, a correlation was achieved which is shown in Equation (7):

$$L_f = 0.91P^{-0.49}(\dot{m}_F / \dot{m}_{pri})^{0.73} \quad (7)$$

The values for the exponent of pressure and $\dot{m}_F / \dot{m}_{pri}$ ratio were -0.49 and 0.73 , respectively, the pressure exponent -0.49 approaches the exponent -0.67 given in [39]. A comparison of the measurement and prediction of L_f with the correlation Equation (7) is presented in Figure 8. Good agreement was observed between measured and the calculated results, which implied the fitting for obtaining the flame length correlation was correct.

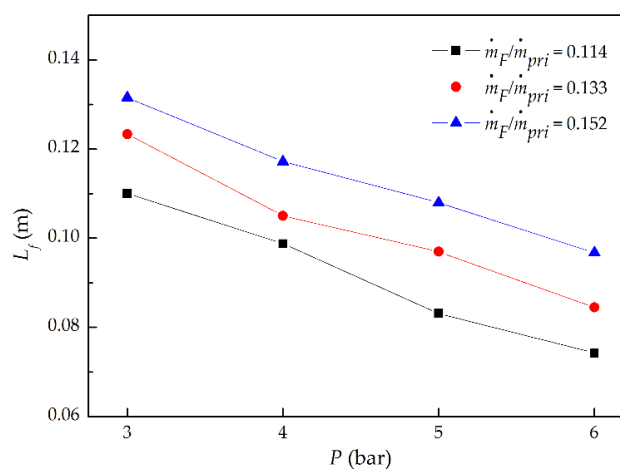


Figure 7. Flame length for combustor pressure under different $\dot{m}_F / \dot{m}_{pri}$ ratios.

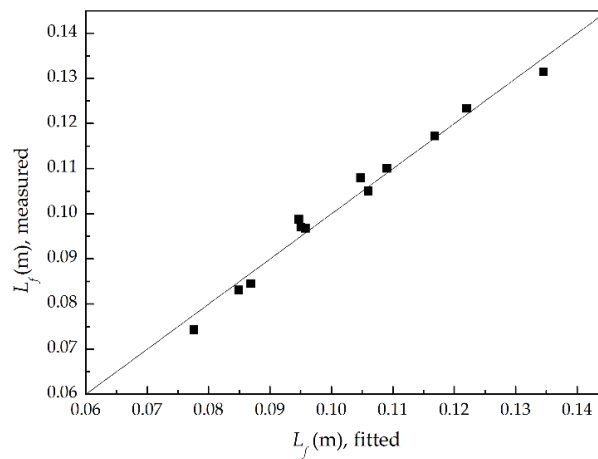


Figure 8. Prediction of flame length from its correlation.

3.2. Exit Gas Oxygen Concentration and Temperature

As shown in Figure 9a, combustor exit gas O₂ volume fraction increased with the increment of pressure when keeping the \dot{m}_F/\dot{m}_{pri} ratio constant. This indicates that less O₂ was consumed at higher pressure, and thus combustion became more incomplete as pressure was increased. This phenomenon corresponded to the decrease in exit temperature with increasing pressure, as shown in Figure 9b, due to the lessened heat release since the O₂ amount taking part in global chemical reactions (8) and/or (9) decreased:



It also can be observed that the exit O₂ volume fraction became smaller with an increase in \dot{m}_F/\dot{m}_{pri} at a given P , which implied more O₂ was consumed through the aforementioned reactions by increasing the fuel. This trend can also be reflected in Figure 9b, which showed the exit temperature increased as the \dot{m}_F/\dot{m}_{pri} ratio was increased because more reaction heat was released due to the increasing fuel and O₂ participating in reactions.

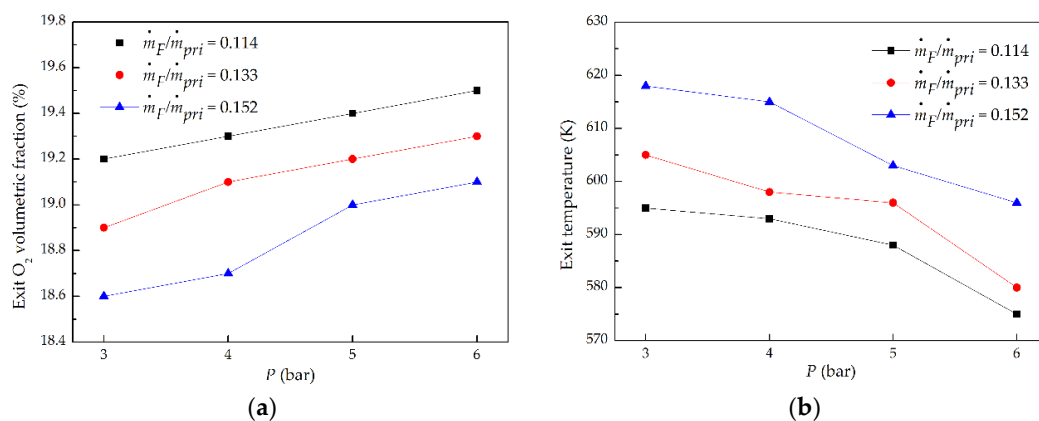


Figure 9. (a) Exit gas O₂ volume fraction; (b) exit temperature.

3.3. Global Flame Residence Time

As mentioned before [26], flame residence time t_R has an important influence on NO formation. The flame residence time t_R can be measured with a global flame residence time t_g , which is defined as Equation (10). The t_g has been used in some previous analyses for NO_x formation [22,40,41],

its definition is based on the consideration that the flame volume V_f is proportional to L_f^3 , as indicated by Equation (11):

$$t_g = L_f^3 / u_e d^2 \quad (10)$$

$$t_R \propto V_f / u_e d^2 \propto L_f^3 / u_e d^2 = t_g \quad (11)$$

To calculate the t_g in present work, the exit velocity u_e needed to be determined. For the sake of convenience and simplicity of analyses in the present situation, the mixture of fuel and primary air is regarded as a nozzle exit fuel \dot{m}_e , i.e., $\dot{m}_e = \dot{m}_F + \dot{m}_{pri}$, and the throat is treated as the nozzle injection exit as stated previously. Then the nozzle exit u_e is obtained by Equation (12):

$$u_e = 4\dot{m}_e / \rho_e \pi d^2 \quad (12)$$

where π stands for circular constant, d is nozzle throat diameter, $d = 0.01$ m, ρ_e is the density of nozzle exit fluid, which can be obtained by ideal gas state Equation (13):

$$\rho_e = P / R_g T \quad (13)$$

where R_g is gas constant, and T represents inlet air temperature, $T = 288$ K.

The calculation result for u_e is shown in Figure 10a; the u_e decreased gradually as pressure increased at a fixed $\dot{m}_F / \dot{m}_{pri}$ ratio, but remained nearly unchanged under a given pressure since the variation value of \dot{m}_F was very small compared to \dot{m}_e . Exit velocity u_e was combined with L_f through Equation (10) to obtain the global flame residence time t_g , as displayed in Figure 10b. One can observe that t_g had a decreasing tendency with the increment of P when $\dot{m}_F / \dot{m}_{pri}$ ratio was fixed, which is attributed to the decreasing L_f (as discussed in the previous section) although u_e decreased as well. However, t_g extended with an increase in $\dot{m}_F / \dot{m}_{pri}$ ratio when P was kept constant, which was explained by the increasing L_f presented in Figure 7. A correlation was obtained on the effects of P and $\dot{m}_F / \dot{m}_{pri}$ on t_g by fitting the experimental data with a power function $y = Cx_1^a x_2^b$, as shown in Equation (14):

$$t_g = 269P^{-0.43} (\dot{m}_F / \dot{m}_{pri})^{2.07} \quad (14)$$

From Equation (14), one can clearly see the influence of P and $\dot{m}_F / \dot{m}_{pri}$ on t_g , t_g decreased with an increase in P ($P^{-0.43}$), but increased significantly with the increasing of $\dot{m}_F / \dot{m}_{pri}$ ($(\dot{m}_F / \dot{m}_{pri})^{2.07}$). A comparison of the measurement and prediction of t_g with correlation Equation (14) is presented in Figure 11. Good agreement was observed between measured and the calculated result. Which implied the fitting for obtaining the global flame residence time correlation was correct.

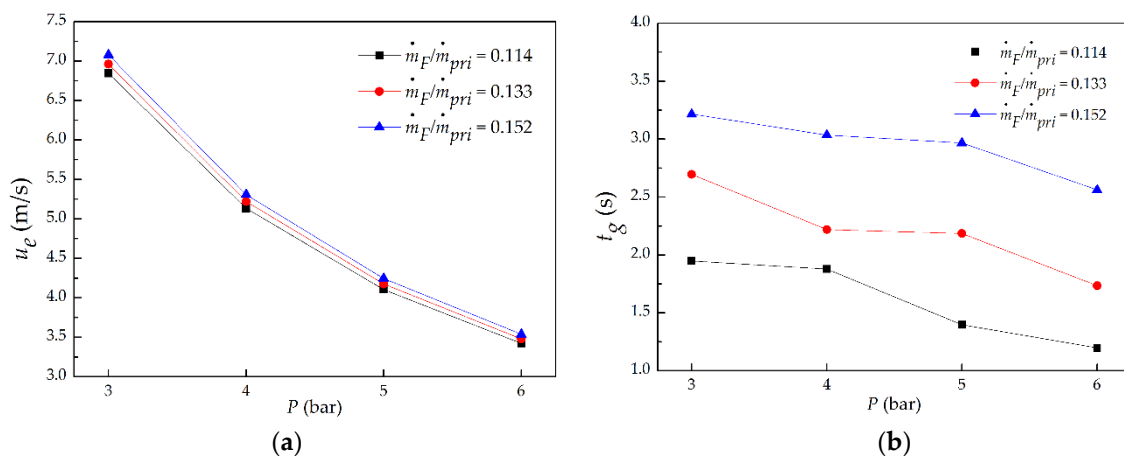


Figure 10. (a) Nozzle exit velocity; (b) global flame residence time.

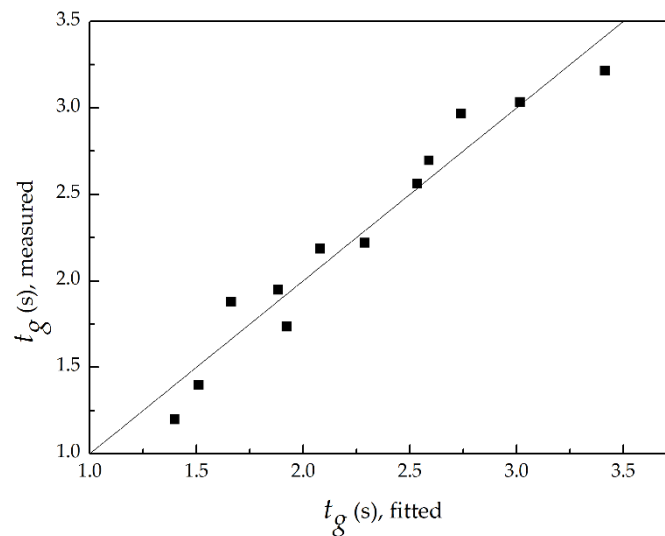


Figure 11. Prediction of global flame residence time from its correlation.

3.4. NO Emission

Thermal NO [42] is the significant pathway for the formation of NO, and its mechanism is described by Equation (15):



Thermal NO formation is controlled largely by flame temperature and increases dramatically with the increment in combustion temperature when the temperature is larger than 1800 K [2]. Therefore, it always dominates the NO formation in high-temperature flames. The residence time in the flame zone also has a significant influence on the thermal NO formation, since the reaction rate of thermal NO is relatively slow [2].

In non-premixed flames, flame surfaces exist where fuel and oxidizer meet in stoichiometric proportions, and thus the temperature of the flame zone is considerably high. The primary formation pathway of NO is thermal NO, which is affected by stoichiometric flame temperature T_{st} and the residence time in the flame zone t_R [26], as can be seen in Equation (4). The T_{st} can be varied with some kinds of operating parameters such as fuel type, inlet air temperature. For all cases in the present experiment, T_{st} was fixed and approached 2300 K, so the effect of T_{st} on NO formation was not considered.

The measured combustor exit NO volumetric fraction and NO emission index EINO are displayed in Figure 12. It can be found that the NO and EINO had a decreasing trend as pressure was raised at a fixed \dot{m}_F/\dot{m}_{pri} ratio, however, increased with the increment of the \dot{m}_F/\dot{m}_{pri} ratio at a given pressure. This was mainly attributed to the effect of the global flame residence time t_g , as shown in Figure 13, the NO and EINO increased since t_g was increased. Combining the results in Figures 10b and 13, the effect of P and \dot{m}_F/\dot{m}_{pri} ratio on NO and EINO can be explained as illustrated in Figure 12.

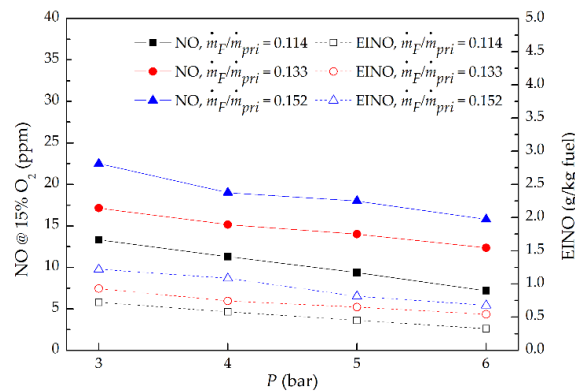


Figure 12. The NO and EINO for combustor pressure under varying \dot{m}_F/\dot{m}_{pri} ratios.

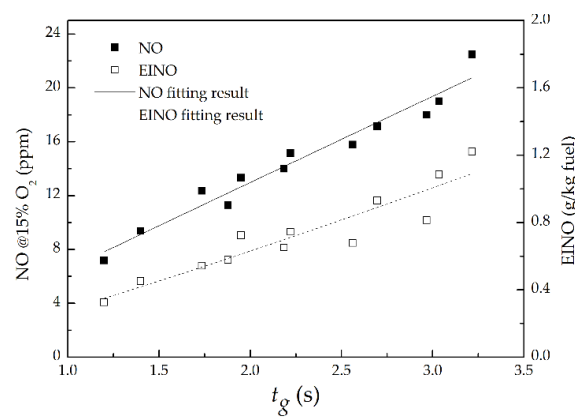


Figure 13. The NO and EINO for the global flame residence time.

The influence of t_g on NO and EINO was examined by fitting the NO and EINO data with a power function $y = Cx^a$. The fitted results are indicated by Equations (16) and (17):

$$\text{NO} = 6.54t_g^{0.99} \quad (16)$$

$$\text{EINO} = 0.28t_g^{1.15} \quad (17)$$

Both equations showed that NO and EINO increased almost proportionally with the increasing t_g ; the increasing rate of EINO is larger slightly than that of NO. Combining the Equations (14), (16) and (17), the NO and EINO correlation with P and \dot{m}_F/\dot{m}_{pri} ratio were derived and expressed as Equations (18) and (19):

$$\text{NO} = 2299P^{-0.47}(\dot{m}_F/\dot{m}_{pri})^{2.17} \quad (18)$$

$$\text{EINO} = 254P^{-0.54}(\dot{m}_F/\dot{m}_{pri})^{2.52} \quad (19)$$

Meanwhile, the data in Figure 12 was also directly fitted with the power function $y = Cx_1^a x_2^b$; the result is characterized by Equations (20) and (21):

$$\text{NO} = 1831P^{-0.53}(\dot{m}_F/\dot{m}_{pri})^{2.02} \quad (20)$$

$$\text{EINO} = 180P^{-0.6}(\dot{m}_F/\dot{m}_{pri})^{2.3} \quad (21)$$

A comparison of the measurements and predictions of NO with the derived correlation Equation (18) and directly fitted correlation (20), respectively, is presented in Figure 14a. Good accordance was found between measured and the calculated result for each correlation.

The results with directly fitted correlation (20) were closer to experimental data than that of derived correlation Equation (18). This should be associated with the accumulated errors as each equation during the deriving process was based on fittings. The same comparison was performed for EINO, using the measured data and Equations (19) and (21), as shown in Figure 14b, the result of comparison was similar to that of NO.

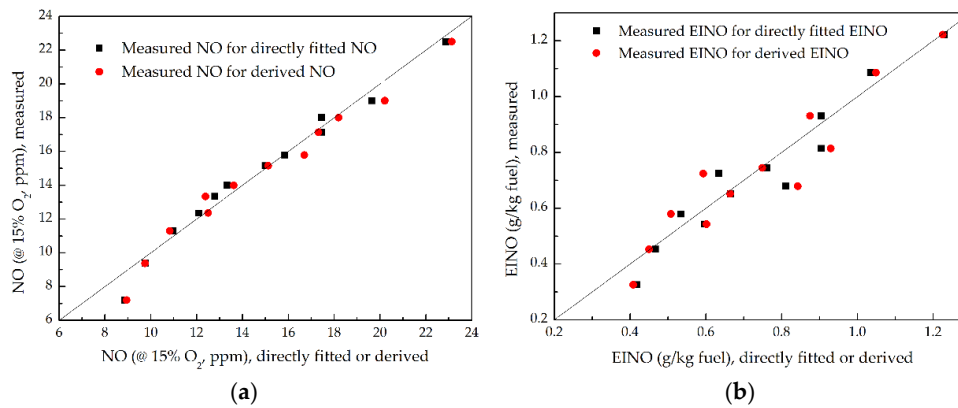


Figure 14. Predictions of NO and EINO from their directly fitted correlation and derived correlation: (a) NO; (b) EINO.

Moreover, in quest of the EINO scaling, the EINO scaled with $(\rho u_e/d)$ is plotted in Figure 15 along with jet Froude number, Fr , as defined in Equation (2). It can be found that EINO $(\rho u_e/d)$ increased with an increase in Fr , and also with an increase in \dot{m}_F/\dot{m}_{pri} ratio. The correlation is presented in Equation (22):

$$\text{EINO}(\rho u_e/d) = 1.23 \times 10^4 Fr^{0.42} (\dot{m}_F/\dot{m}_{pri})^{2.08} \quad (22)$$

The prediction of EINO $(\rho u_e/d)$ with correlation Equation (22) was compared to the measurement as depicted in Figure 16. Good accordance was found between measured and the calculated results. This implied the fitting for obtaining the correlation Equation (22) is appropriate. In previous NO scaling with pure fuel, EINO $(\rho u_e/d)$ was proportional to $Fr^{0.6}$ [19–22], the present NO scaling with the addition of primary air to fuel indicated EINO $(\rho u_e/d)$ was proportional to $Fr^{0.42}$, the exponent decreased from 0.6 to 0.42. This decline indicated that addition of primary air in the fuel could cause a decrease in the exponent of Fr power function, which may due to the decrease in flame length when primary air is added to fuel [43], thus affecting the flame residence time and NO.

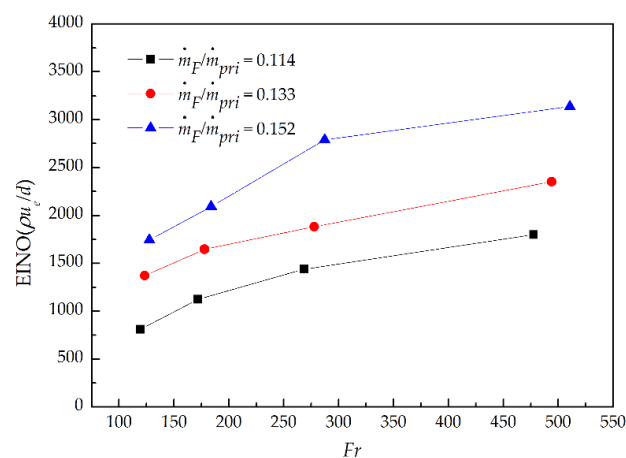


Figure 15. Variation of EINO $(\rho u_e/d)$ with Fr under varying \dot{m}_F/\dot{m}_{pri} ratios.

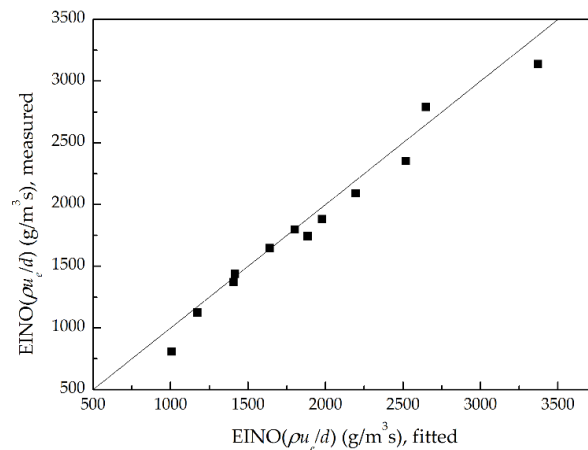


Figure 16. Prediction of EINO ($\rho u_e/d$) from its correlation.

3.5. CO Emission

The formation reaction of CO is shown in Equations (8) and (9), where Equation (8) is the CO production reaction, and Equation (9) is the CO consumption reaction. The presence of the CO in the exhaust gas in large quantities is a reflection of incomplete combustion of fuel caused by insufficient burning rates in flame zone, inadequate mixing of fuel and air, the chilling influence of liner coolant, and/or insufficient residence time.

In present measurement, the impacts of combustor pressure under different \dot{m}_F/\dot{m}_{pri} ratios on CO and EICO are presented in Figure 17. The CO emission index EICO is defined as the ratio of the mass rate of CO produced to the mass of fuel supplied, as given by Equation (23)

$$\text{EICO} = \dot{m}_{\text{CO}}/\dot{m}_F \quad (23)$$

The results showed that the CO and EICO decreased gradually with the raise in P at a fixed \dot{m}_F/\dot{m}_{pri} ratio. This can be attributed to two reasons: one of the reasons is that the flame volume got shrunk at higher P , leading to less CH_4 captured and burned in a timely way by the flame, therefore resulting in the less CO formation through Equation (8). This also corresponded to the less O_2 consumption at higher P as mentioned before. Another reason is that the increasing pressure accelerated chemical reaction kinetics to promote the conversion of CO to CO_2 through the Equation (9). Furthermore, the dissociation was suppressed as high pressure favors CO_2 over CO and O_2 [44].

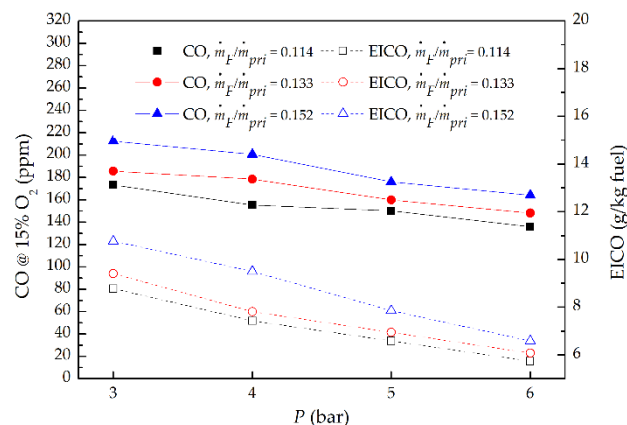


Figure 17. The CO and EINO for combustor pressure under varying \dot{m}_F/\dot{m}_{pri} ratios.

It also can be observed that CO and EICO increased with the increment in \dot{m}_F/\dot{m}_{pri} ratio at a given P , which is explained by the escalating CO formation through Equation (8) as more CH_4 participated in the combustion. Fitting the data in Figure 17 with the power function $y = Cx_1^a x_2^b$, the correlations for the influences of P and \dot{m}_F/\dot{m}_{pri} ratio on CO and EICO are described by Equations (24) and (25):

$$\text{CO} = 1196P^{-0.35}(\dot{m}_F/\dot{m}_{pri})^{0.72} \quad (24)$$

$$\text{EICO} = 65P^{-0.4}(\dot{m}_F/\dot{m}_{pri})^{0.75} \quad (25)$$

The prediction of CO with the correlation in Equation (24) was compared to the measurement as shown in Figure 18a. Good accordance is found between measured and the calculated results. This implied the fitting for obtaining the correlation Equation (24) is appropriate. The same comparison was performed for EICO, using the measured data and Equation (25), as shown in Figure 18b, the difference between experimental data and predicting the result is reasonable.

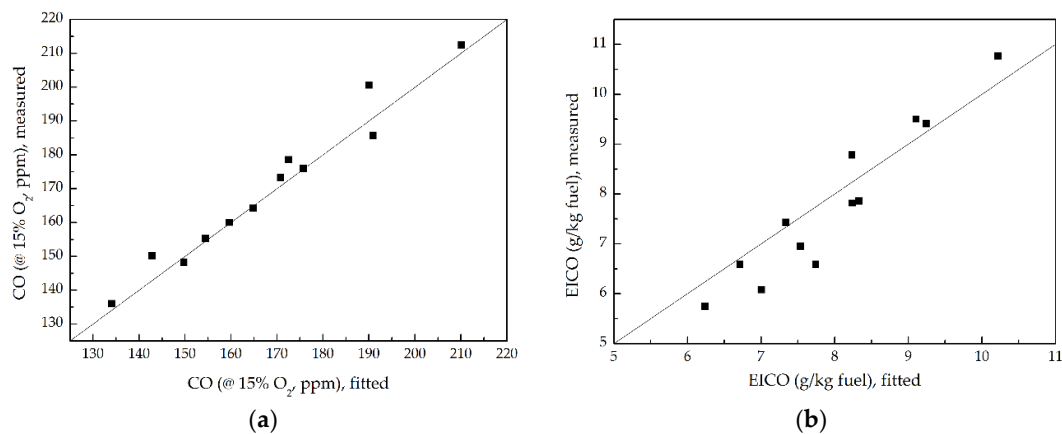


Figure 18. Predictions of CO and EICO from their correlations: (a) CO; (b) EICO.

The correlation Equations (20), (21) and (24), (25) are similar to Equation (5) in terms of their forms, they are composed of a product of the power functions of parameters. The NO and CO correlations obtained in present paper may help in understanding the emissions behavior of non-premixed flame with the partial premixing of fuel and primary air at elevated pressure.

4. Conclusions

The NO and CO emissions for a swirl convergent-divergent nozzle were examined experimentally at elevated combustor pressure; The NO and CO correlations were obtained in terms of pressure P and fuel to primary air ratio \dot{m}_F/\dot{m}_{pri} . The flame shape and length, exit gas oxygen concentration and temperature, and global flame residence time were also determined to analyze the NO and CO characteristics. The main findings of the present paper include:

- (1) With the increment of P at a fixed \dot{m}_F/\dot{m}_{pri} ratio, flame volume became smaller, and flame length decreased proportionally to $P^{-0.49}$; while increasing \dot{m}_F/\dot{m}_{pri} ratio at a given P , flame volume became larger, and flame length increased proportionally to $(\dot{m}_F/\dot{m}_{pri})^{0.73}$.
- (2) With the rise in P at a fixed \dot{m}_F/\dot{m}_{pri} ratio, combustor exit gas O_2 volume fraction became larger, and exit temperature decreased; with the increasing of \dot{m}_F/\dot{m}_{pri} ratio at a given P , exit O_2 volume fraction became smaller, and exit temperature increased.
- (3) With the increasing P at a fixed \dot{m}_F/\dot{m}_{pri} ratio, the global flame residence time lessened proportionally to $P^{-0.43}$; with the increasing of \dot{m}_F/\dot{m}_{pri} ratio at a given P , the global flame residence time extended proportionally to $(\dot{m}_F/\dot{m}_{pri})^{2.07}$.

- (4) As P increased at a fixed \dot{m}_F/\dot{m}_{pri} ratio, the NO and EINO decreased proportionally to $P^{-0.53}$ and $P^{-0.6}$, respectively, but increased proportionally to $(\dot{m}_F/\dot{m}_{pri})^{2.02}$ and $(\dot{m}_F/\dot{m}_{pri})^{2.3}$ separately as the \dot{m}_F/\dot{m}_{pri} ratio increased at a given P . This is mainly attributed to the influence of global flame residence time; the NO and EINO nearly increased proportionally with the increasing global flame residence time.
- (5) With the addition of primary air in fuel, the EINO scaling $EINO(\rho u_e/d)$ was proportional to $Fr^{0.42}$. Which indicated the dilution of primary air to fuel could cause a decrease in the exponent of Fr power function comparing with $Fr^{0.6}$ for pure fuel.
- (6) As P increased at a fixed \dot{m}_F/\dot{m}_{pri} ratio, the CO and EICO decreased proportionally to $P^{-0.35}$ and $P^{-0.4}$ respectively, due to the increased unburned methane and high pressure which accelerated chemical reaction kinetics to promote the conversion of CO to CO_2 . However, the CO and EICO enlarged proportionally to $(\dot{m}_F/\dot{m}_{pri})^{0.72}$ and $(\dot{m}_F/\dot{m}_{pri})^{0.75}$ separately as \dot{m}_F/\dot{m}_{pri} ratio increased at a given P , due to the increased fuel participating in combustion.

Author Contributions: Z.X. and Z.F. conceived and designed the experiments; Z.X., X.H., and Y.J. performed the experiments; Z.X. and X.H. analyzed the data; Z.X. and X.H. contributed reagents/materials/analysis tools; Z.X. and Syed Waqas Sabir wrote the paper.

Acknowledgments: This research was supported by Beijing Natural Science Foundation (Grant No. 3162030).

Conflicts of Interest: The authors declare no conflict of interest.

Appendix A

Table A1. The NO and CO correlations in the open literature. Scale equations.

Reference	Model Equation	Model Parameter
Rizk and Mongia [45]	$EINO_x = 15 \times 10^{14} \cdot t_{res}^{0.5} \cdot \exp(-71,100/T_{fl}) \cdot P_3^{-0.03} \cdot (\Delta P_3/P_3)^{-0.5}$	$T_{res}, T_{fl}, P_3, \Delta P_3$
Lipfert [46]	$EINO_x = 0.17282 \cdot \exp(0.00676593T_3)$	T_3
AECMA [46]	$EINO_x = 2 + 28.5 \cdot (P_3/3100)^{0.5} \exp((T_3 - 825)/250)$	P_3, T_3
Becker et al. [47]	$NO_x(ppm) = 5.73 \times 10^{-6} \cdot \exp(0.00833T_{fl})P_3^{0.5}$	T_{fl}, P_3
Odgers and Kretschmer [44]	$EINO_x = 29 \cdot \exp(-21,670/T_{fl})P_3^{0.66}(1 - \exp(-250t_{form}))$	T_{fl}, P_3, t_{form}
Lefebvre [26]	$EINO_x = 0.459 \times 10^{-8} \cdot P_3^{0.25} \cdot F \cdot t_{res} \cdot \exp(0.01(T_{fl} + 273))$	P_3, F, t_{res}, T_{fl}
Rokke et al. [27]	$EINO_x = 1.46P^{1.42}\dot{m}_{air}^{0.3}f_{far}^{0.72}$	$\dot{m}_{air}, f_{far} = \dot{m}_{fuel}/\dot{m}_{ai}$
General Electric [48]	$EINO_x = 2.2 + 0.1235 \cdot P_3^{0.4} \cdot \exp(T_3/194.4 - hum \cdot 1000/53.2)$	P_3, T_3, hum
AERONOX [48]	$EINO_x = 1.5 \cdot (P_3/100)^{0.6} \cdot \exp(-600/T_4) \cdot t_{res}^{0.7}$	P_3, T_4, t_{res}
Lefebvre [26]	$EICO = \frac{0.333 \times 10^{10} \cdot \exp(-0.00275 \cdot T_{PZ})}{F \cdot P_3^{1.5} \cdot (t_{res} - 0.55 \cdot t_{evap}) \cdot (\Delta P_3/P_3)^{0.5}}$	$T_{PZ}, F, P_3, t_{res}, t_{evap}, \Delta P_3$
Rizk and Mongia [49]	$EICO = 0.18 \cdot 10^9 \exp(7800/T_{PZ})/P^2(t - 0.4t_e)(\Delta P/P)^{0.5}$	$T_{PZ}, P, t, t_e, \Delta P$

References

- Li, M.; Tong, Y.; Klingmann, J.; Thern, M. Experimental study of hydrogen addition effects on a swirl-stabilized methane-air flame. *Energies* **2017**, *10*, 1769. [[CrossRef](#)]
- Miller, J.A.; Bowman, C.T. Mechanism and modeling of nitrogen chemistry in combustion. *Prog. Energy Combust. Sci.* **1989**, *15*, 287–338. [[CrossRef](#)]
- Lefebvre, A.H.; Ballal, D.R. Emissions. In *Gas Turbine Combustion: Alternative Fuels and Emissions*; CRC Press: Boca Raton, FL, USA, 2010; pp. 366–382, ISBN 9781420086058.
- Boyce, M.P. Theoretical and Actual Cycle Analyses. In *Gas Turbine Engineering Handbook*; Elsevier Inc.: Waltham, MA, USA, 2012; p. 90, ISBN 9780123838421.
- Liakos, H.H.; Founti, M.A.; Markatos, N.C. Relative importance of combustion mechanisms in industrial premixed flames under high pressure. *Appl. Therm. Eng.* **2000**, *20*, 925–940. [[CrossRef](#)]
- Gomez-Ramirez, D.; Kedukodi, S.; Gadiraju, S.; Ekkad, S.V.; Moon, H.-K.; Kim, Y.; Srinivasan, R. Gas turbine combustor rig development and initial observations at cold and reacting flow conditions. In Proceedings of the ASME Turbo Expo 2016: Turbomachinery Technical Conference and Exposition, Seoul, Korea, 13–17 June 2016; Volume 5B.

7. Han, D.S.; Kim, G.B.; Kim, H.S.; Jeon, C.H. Experimental study of NO_x correlation for fuel staged combustion using lab-scale gas turbine combustor at high pressure. *Exp. Therm. Fluid Sci.* **2014**, *58*, 62–69. [[CrossRef](#)]
8. Correa, S.M. A Review of NO_x Formation Under Gas-Turbine Combustion Conditions. *Combust. Sci. Technol.* **1993**, *87*, 329–362. [[CrossRef](#)]
9. Bhargava, A.; Kendrick, D.W.; Casleton, K.H.; Maloney, D.J.; Colket, M.B.; Sowa, W.A. Pressure effect on NO_x and CO emissions in industrial gas turbines. In Proceedings of the ASME Turbo Expo 2000: Power for Land, Sea, and Air, Munich, Germany, 8–11 May 2000; Volume 2.
10. Göke, S.; Schimek, S.; Terhaar, S.; Reichel, T.; Göckeler, K.; Krüger, O.; Fleck, J.; Griebel, P.; Paschereit, C.O. Influence of Pressure and Steam Dilution on NO_x and CO Emissions in a Premixed Natural Gas Flame. *J. Eng. Gas Turbines Power* **2014**, *136*, 091508. [[CrossRef](#)]
11. Wang, H.; Lei, F.; Shao, W.; Zhang, Z.; Liu, Y.; Xiao, Y. Experimental and numerical studies of pressure effects on syngas combustor emissions. *Appl. Therm. Eng.* **2016**, *102*, 318–328. [[CrossRef](#)]
12. Pillier, L.; Idir, M.; Molet, J.; Matynia, A.; Persis, S. De Experimental study and modelling of NO_x formation in high pressure counter-flow premixed CH₄/air flames. *Fuel* **2015**, *150*, 394–407. [[CrossRef](#)]
13. Shuman, T. NO_x and CO Formation for Lean-Premixed Methane-Air Combustion in a Jet-Stirred Reactor Operated at Elevated Pressure. Ph.D. Thesis, University of Washington, Seattle, WA, USA, 2000.
14. Steel, R.C.; Jarrett, A.C.; Malte, P.C.; Tonouchi, J.H.; Nicol, D.G. Variables Affecting NO_x Formation in Lean-Premixed Combustion. *J. Eng. Gas Turbines Power* **1997**, *119*, 102–107. [[CrossRef](#)]
15. Biagioli, F.; Gütthe, F. Effect of pressure and fuel-air unmixedness on NO_x emissions from industrial gas turbine burners. *Combust. Flame* **2007**, *151*, 274–288. [[CrossRef](#)]
16. Leonard, G.; Stegmaier, J. Development of an Aeroderivative Gas Turbine Dry Low Emissions Combustion System. *J. Eng. Gas Turbines Power* **1994**, *116*, 542. [[CrossRef](#)]
17. Røkke, N.A.; Hustad, J.E.; Sønju, O.K.; Williams, F.A. Scaling of nitric oxide emissions from buoyancy-dominated hydrocarbon turbulent-jet diffusion flames. *Symp. Combust.* **1992**, *24*, 385–393. [[CrossRef](#)]
18. Turns, S.R. Understanding NO_x formation in nonpremixed flames: Experiments and modeling. *Prog. Energy Combust. Sci.* **1995**, *21*, 361–385. [[CrossRef](#)]
19. Newbold, G.J.R.; Nathan, G.J.; Nobes, D.S.; Turns, S.R. Measurement and prediction of NO_x emissions from unconfined propane flames from turbulent-jet, bluff-body, swirl, and precessing jet burners. *Proc. Combust. Inst.* **2000**, *28*, 481–487. [[CrossRef](#)]
20. Kiran, D.Y.; Mishra, D.P. Experimental studies of flame stability and emission characteristics of simple LPG jet diffusion flame. *Fuel* **2007**, *86*, 1545–1551. [[CrossRef](#)]
21. Santos, A.; Costa, M. Reexamination of the scaling laws for NO_x emissions from hydrocarbon turbulent jet diffusion flames. *Combust. Flame* **2005**, *142*, 160–169. [[CrossRef](#)]
22. Costa, M.; Parente, C.; Santos, A. Nitrogen oxides emissions from buoyancy and momentum controlled turbulent methane jet diffusion flames. *Exp. Therm. Fluid Sci.* **2004**, *28*, 729–734. [[CrossRef](#)]
23. Szegö, G.G.; Dally, B.B.; Nathan, G.J. Scaling of NO_x emissions from a laboratory-scale mild combustion furnace. *Combust. Flame* **2008**, *154*, 281–295. [[CrossRef](#)]
24. Tsalavoutas, A.; Kelaidis, M.; Thoma, N. Correlations adaptation for optimal emissions prediction. In Proceedings of the ASME Turbo Expo 2007: Power for Land, Sea, and Air, Montreal, QC, Canada, 14–17 May 2007; pp. 545–555.
25. Chandrasekaran, N.; Guha, A. Study of Prediction Methods for NO_x Emission from Turbofan Engines. *J. Propuls. Power* **2012**, *28*, 170–180. [[CrossRef](#)]
26. Rizk, N.K.; Mongia, H.C. Semianalytical Correlations for NO_x, CO, and UHC Emissions. *J. Eng. Gas Turbines Power* **1993**, *115*, 612. [[CrossRef](#)]
27. Røkke, N.A.; Hustad, J.E.; Bergs, B. Pollutant Emissions From Gas Fired Turbine Engines in Offshore Practice: Measurements and Scaling. In Proceedings of the ASME 1993 International Gas Turbine and Aeroengine Congress and Exposition, Cincinnati, OH, USA, 24–27 May 1993; p. V03AT15A021.
28. Li, L.; Lin, Y.; Fu, Z.; Zhang, C. Emission characteristics of a model combustor for aero gas turbine application. *Exp. Therm. Fluid Sci.* **2016**, *72*, 235–248. [[CrossRef](#)]
29. Kroniger, D.; Wirsum, M.; Horikawa, A.; Okada, K.; Kazari, M. NO_x Correlation for an Industrial 10 MW Non-Premixed Gas Turbine Combustor for High Hydrogen Fuels. In Proceedings of the ASME Turbo Expo 2016: Turbomachinery Technical Conference and Exposition, Seoul, Korea, 13–17 June 2016; Volume 4A, p. V04AT04A012.

30. Domkundwar, V.M.; Sriramulu, V.; Gupta, M.C. Analysis of swirling recirculating reacting turbulent jets passing through diffusers. *Combust. Flame* **1978**, *33*, 241–249. [[CrossRef](#)]
31. Cheng, T.S.; Chao, Y.C.; Wu, D.C.; Yuan, T.; Lu, C.C.; Cheng, C.K.; Chang, J.M. Effects of fuel-air mixing on flame structures and NO_x emissions in swirling methane jet flames. *Symp. (Int.) Combust.* **1998**, *27*, 1229–1237. [[CrossRef](#)]
32. Terasaki, T.; Hayashi, S. The effects of fuel-air mixing on NO_x formation in non-premixed swirl burners. *Symp. Combust.* **1996**, *26*, 2733–2739. [[CrossRef](#)]
33. Mansour, M.S. A Concentric Flow Conical Nozzle Burner for Highly Stabilized Partially Premixed Flames. *Combust. Sci. Technol.* **2000**, *152*, 115–145. [[CrossRef](#)]
34. El-Mahallawy, F.; Abdelhafez, A.; Mansour, M.S. Mixing and nozzle geometry effects on flame structure and stability. *Combust. Sci. Technol.* **2007**, *179*, 249–263. [[CrossRef](#)]
35. Mansour, M.S.; Elbaz, A.M.; Samy, M. The stabilization mechanism of highly stabilized partially premixed flames in a concentric flow conical nozzle burner. *Exp. Therm. Fluid Sci.* **2012**, *43*, 55–62. [[CrossRef](#)]
36. Liu, X.; Elbaz, A.M.; Gong, C.; Bai, X.S.; Zheng, H.T.; Roberts, W.L. Effect of burner geometry on swirl stabilized methane/air flames: A joint LES/OH-PLIF/PIV study. *Fuel* **2017**, *207*, 533–546. [[CrossRef](#)]
37. Samaniego, J.-M.; Egolfopoulos, F.N.; Bowman, C.T. CO₂* Chemiluminescence in Premixed Flames. *Combust. Sci. Technol.* **1995**, *109*, 183–203. [[CrossRef](#)]
38. Hu, L.; Wang, Q.; Delichatsios, M.; Tang, F.; Zhang, X.; Lu, S. Flame height and lift-off of turbulent buoyant jet diffusion flames in a reduced pressure atmosphere. *Fuel* **2013**, *109*, 234–240. [[CrossRef](#)]
39. Most, J.M.; Mandin, P.; Chen, J.; Joulain, P.; Durox, D.; Ferlande-Pello, A.C. Influence of gravity and pressure on pool fire-type diffusion flames. *Symp. Combust.* **1996**, *26*, 1311–1317. [[CrossRef](#)]
40. Kim, S.-H.; Yoon, Y.; Jeung, I.-S. Nitrogen oxides emissions in turbulent hydrogen jet non-premixed flames: Effects of coaxial air and flame radiation. *Proc. Combust. Inst.* **2000**, *28*, 463–471. [[CrossRef](#)]
41. Driscoll, J.F.; Chen, R.-H.; Yoon, Y. Nitric oxide levels of turbulent jet diffusion flames: Effects of residence time and damkohler number. *Combust. Flame* **1992**, *88*, 37–49. [[CrossRef](#)]
42. Zeldovitch, J. The oxidation of nitrogen in combustion and explosions. *Eur. Phys. J. A Hadrons Nucl.* **1946**, *21*, 577–628.
43. Turns, S.R.; Myhr, F.H.; Bandaru, R.V.; Maund, E.R. Oxides of nitrogen emissions from turbulent jet flames: Part II-Fuel dilution and partial premixing effects. *Combust. Flame* **1993**, *93*, 255–269. [[CrossRef](#)]
44. Lefebvre, A.H. The Role of Fuel Preparation in Low-Emission Combustion. *J. Eng. Gas Turbines Power* **1995**, *117*, 617–654. [[CrossRef](#)]
45. Mongia, H.C.; Dodds, W. Low emissions propulsion engine combustor technology evolution past, present and future. In Proceedings of the 24th Congress of International Council of the Aeronautical Sciences, Yokohama, Japan, 29 August–3 September 2004; pp. 2004–2609.
46. Green, J.E. Greener by design—The technology challenge. *Aeronaut. J.* **2002**, *106*. [[CrossRef](#)]
47. Becker, T.; Perkavec, M.A. The Capability of Different Semianalytical Equations for Estimation of NO_x Emissions of Gas Turbines. In Proceedings of the ASME 1994 International Gas Turbine and Aeroengine Congress and Exposition, The Hague, The Netherlands, 13–16 June 1994; p. V003T06A020.
48. Tilston, J.; Larkman, J.; Plohr, M.; Doepelheuer, A.; Lischer, T.; Zarzalis, N. *Future Engine Cycle Prediction and Emissions Study*; EU FP5 CYPRESS, Final Publishable Report, Contract; European Commission: Brussels, Belgium, 2003; G4RD-CT: 2000-00383.
49. Rizk, N.; Mongia, H. Emissions predictions of different gas turbine combustors. In Proceedings of the 32nd Aerospace Sciences Meeting and Exhibit, Reno, NV, USA, 10–13 January 1994; p. 118.

